

Gate-tunable valley currents, nonlocal resistances, and valley accumulation in bilayer graphene nanostructures

Mohammadhadi Azari and George Kirczenow

Department of Physics, Simon Fraser University, Burnaby, British Columbia, Canada V5A 1S6

(Received 13 December 2016; revised manuscript received 26 March 2017; published 25 May 2017)

Using the Büttiker-Landauer formulation of transport theory in the linear response regime, the valley currents and nonlocal resistances of bilayer graphene nanostructures with broken inversion symmetry are calculated. It is shown that broken inversion symmetry in bilayer graphene nanostructures leads to striking enhancement of the nonlocal four-terminal resistance and to valley currents several times stronger than the conventional electric current when the Fermi energy is in the spectral gap close to the energy of Dirac point. The scaling relation between local and nonlocal resistances is investigated as the gate voltage varies at zero Fermi energy and a power law is found to be satisfied. The valley velocity field and valley accumulation in four-terminal bilayer graphene nanostructures are evaluated in the presence of inversion symmetry breaking. The valley velocity and nonlocal resistance are found to scale differently with the applied gate voltage. The unit cell-averaged valley accumulation is found to exhibit a dipolar spatial distribution consistent with the accumulation arising from the valley currents. We define and calculate a *valley capacitance* that characterizes the valley accumulation response to voltages applied to the nanostructure's contacts.

DOI: [10.1103/PhysRevB.95.195424](https://doi.org/10.1103/PhysRevB.95.195424)

I. INTRODUCTION

Graphene is a two-dimensional one-atom-thick layer of carbon atoms arranged on a honeycomb lattice. Bilayer graphene consists of two electronically coupled single graphene layers. Excellent electrical and thermal conductivity [1–5] at room temperature, high strength, flexibility, and transparency [6] are properties common to bilayer and monolayer of graphene that make them appropriate candidates for potential applications in future technology. In both monolayer and bilayer graphene the conduction (valence) band has local minima (maxima) called “valleys.” As a consequence, the charge carriers in both materials have a degree of freedom, referred to as the “valley degree of freedom” which is controllable electrically when inversion symmetry is broken. Although the electronic coupling between the two carbon layers that make up the graphene bilayer is relatively weak, it nevertheless results in important differences between the electronic structures of bilayer and monolayer graphene. Specifically, in contrast to the low-energy linear dispersion of monolayer graphene, the low energy dispersion of bilayer graphene is quadratic. The band structures of monolayer and bilayer graphene both possess interesting topological properties related to the Berry phase and Berry curvature [7]. The breaking of inversion symmetry in both materials results in nonzero Berry curvature $\Omega_{\mathbf{k}}$ close to Dirac points. Based on semiclassical theories of electron transport [7–9], a nonzero Berry curvature affects the electron velocity \mathbf{v} in the presence of an electric field \mathbf{E} according to

$$\mathbf{v}_{\mathbf{k}} = \frac{1}{\hbar} \frac{\partial \epsilon_{\mathbf{k}}}{\partial \mathbf{k}} + \dot{\mathbf{k}} \times \Omega_{\mathbf{k}}, \quad (1)$$

where $\epsilon_{\mathbf{k}}$ is the energy of a Bloch state with wave vector \mathbf{k} and $\hbar \dot{\mathbf{k}} = q_e \mathbf{E}$ in the absence of magnetic fields. Consequently, the Berry curvature $\Omega_{\mathbf{k}}$ can be exploited as a tool to manipulate the valley degree of freedom in these materials when the inversion symmetry is broken since $\Omega_{\mathbf{k}}$ points in opposite directions in the two valleys. In particular, Eq. (1) implies a difference in velocity of electrons that belong to different valleys if

the inversion symmetry is broken. This different response of electrons in different valleys to electric fields may be utilized in future valleytronic devices. However, it should be noted that the inversion symmetry breaking (that is crucial for valleytronics based on the Berry curvature mechanism) is achieved in fundamentally different ways for monolayer and bilayer graphene: For monolayer graphene it is imposed by applying a staggered potential that is different at the two atoms of the graphene unit cell. This is done in practice by placing the graphene monolayer on a boron nitride substrate [10]. By contrast, for bilayer graphene the inversion symmetry is broken by applying potentials that are uniform throughout each of the monolayers that make up the bilayer but differ between the two monolayers. This is done by dual electrostatic gating [11,12].

Recently, experiments have been carried out, measuring nonlocal four-terminal resistances of monolayer graphene on boron nitride [10] and of dual gate-biased bilayer graphene (BLG) in a Hall bar configuration [11,12]. In these experiments the inversion symmetries of the materials were broken as described above so as to induce Berry curvature as well as a band gap. Strong enhancement of the nonlocal (four-terminal) resistance R_{NL} was observed [10–12] when the Fermi level passed the energy of Dirac points in the insulating regime. Gorbachev *et al.* [10] and Shimazaki *et al.* [11] interpreted the enhancement of R_{NL} that they observed in symmetry broken monolayer and bilayer graphene, respectively, as an effect due to valley currents, basing their reasoning on the semiclassical theories of electron transport embodied in Eq. (1). They argued that the anomalous velocity [second term on the right-hand side in Eq. (1)] generates pure valley currents transverse to the electric current which is flowing within the sample between current contacts. These valley currents then flow between the voltage probes within the sample and result in a potential difference and enhancement of the nonlocal resistance [10,11].

However, the enhanced nonlocal resistance was observed in the insulating regime [10–12], where the Fermi level was in the energy gap opened in the electronic band structures by the respective symmetry breaking mechanisms. Therefore the

electron transport mechanism involved was quantum tunneling. Hence, as has been discussed for monolayer graphene nanostructures [13], the applicability of semiclassical theories of electron transport [Eq. (1)] to the observed enhancement of nonlocal resistance in the insulating regime is questionable because quantum tunneling has no classical analog. In addition, it has been pointed out [13] that, according to Büttiker-Landauer theory [14], the Berry curvature mechanism embodied in the anomalous velocity term in Eq. (1) cannot affect nonlocal resistances such as R_{NL} in the linear response regime. Therefore, any enhancement of R_{NL} in the linear response regime should not be regarded as evidence of valley currents arising from the topological Berry curvature (anomalous velocity) mechanism. On the other hand, fully quantum mechanical computer simulations based on Büttiker-Landauer theory, carried out for monolayer graphene nanostructures, have shown [13] that in the linear response regime, inversion symmetry breaking gives rise to both strongly enhanced nonlocal resistances and strong valley currents when the Fermi level is within the energy gap around the Dirac point. The valley currents found in those simulations did not arise from the anomalous velocity term in Eq. (1) but were the direct result of electron injection into the monolayer graphene nanostructure [13].

The previous computer simulations [13] were confined to monolayer graphene nanostructures. However, as has been discussed above, the physics of bilayer graphene differs in important ways from that of monolayer graphene with regard to both the electronic structure and the symmetry breaking mechanism. Therefore, whether analogous behavior of the nonlocal resistance and valley currents should occur in bilayer graphene has remained an open question. From a practical perspective, the gate tunability of the symmetry breaking in bilayer graphene by application of a perpendicular electric field (being not available for monolayer graphene) is an advantage for bilayer graphene as a potential candidate for applications in future valleytronics. Also while experimental measurements of nonlocal resistances of symmetry broken bilayer graphene have been reported [11,12] no fully quantum mechanical calculations of nonlocal resistances for this material are available in the literature. It is therefore of interest to explore the behavior of valley currents and nonlocal resistances in bilayer graphene nanostructures theoretically by means of fully quantum mechanical Büttiker-Landauer calculations. Such calculations are reported in the present article.

Despite the fundamental differences (described above) between the electronic structures and symmetry breaking mechanisms of bilayer and monolayer graphene, we find some *qualitative* similarities between the valley currents and nonlocal resistances of the two systems. Specifically, we find that in bilayer graphene nanostructures (in common with monolayer nanostructures [13]) inversion symmetry breaking induces strong enhancement of the nonlocal resistance and strong valley currents transverse to the electric current in the linear response regime when the Fermi level is in the energy gap that is opened by the symmetry breaking. Also, in common with the monolayer case [13], we find the valley currents in the bilayer nanostructures to be chiral and to be located predominantly near the edges of the bilayer graphene where electrons are injected from electrodes when the Fermi level is in the energy gap.

However, in the present article we also study quantitatively the scaling of the valley velocity and nonlocal and local resistances with the dual gate voltage V_g that is responsible for the symmetry breaking in bilayer graphene; such studies are not possible for monolayer graphene where symmetry breaking is imposed instead by the presence of a boron nitride substrate. We investigate the scaling relations of the local resistance R_L and nonlocal resistance and valley currents in ballistic nanostructures in the linear response regime at zero temperature as the gate voltage varies for $E_F = 0$. We find the power law $R_{NL} \propto R_L^\alpha$ to be satisfied with $\alpha = 2.19$ in our ballistic bilayer nanostructures, whereas $\alpha \sim 2.77$ has been observed experimentally in bilayer graphene in the diffusive regime [12]. While theoretical predictions for α have not been available previously for bilayer graphene, $\alpha = 3$ has been predicted for diffusive spin Hall systems [15]. Interestingly, we find the normalized valley current to scale linearly with gate voltage for low gate voltages while the nonlocal resistance scales quadratically starting from a nonzero value at zero gate voltage.

We also introduce and calculate the *valley accumulation* and *valley capacitance* associated with valley currents. While there have been previous theoretical studies of valley currents induced in graphene in various ways [13,16–23], whether and to what extent the valley currents result in valley accumulation of electrons, i.e., in differing electron populations of the different valleys, has remained unclear. To our knowledge, there has been no estimate of the valley accumulation or of its spatial distribution resulting from valley currents in any graphene device. This is despite the central role that valley accumulation is expected to play in future valleytronic devices whose operation, by definition, depends on imbalances between the electron populations of the different valleys. We therefore investigate the valley accumulation of electrons associated with valley currents in bilayer graphene nanostructures and report our results here. We find the valley accumulation to typically have opposite signs on the two carbon atoms of the unit cell of each graphene monolayer of the bilayer. After averaging over the unit cell, we find the cell-averaged valley accumulation to exhibit a dipolar spatial distribution. The dipole is oriented along the overall direction of the valley current flow, consistent with the valley current giving rise to the dipolar accumulation. In order to develop an intuitively appealing figure of merit for the magnitude of the response of the valley accumulation to voltages applied to the contacts of graphene nanostructures in the linear response regime we define a *valley capacitance* and evaluate it for a bilayer graphene nanostructure with broken inversion symmetry.

The present model of bilayer graphene with broken inversion symmetry, the formalism of Büttiker-Landauer theory, the Lippmann-Schwinger equation, and their application in calculations of the nonlocal resistance, valley currents, and valley accumulation are described in Sec. II. Our results are presented in Sec. III. We summarize and discuss our main conclusions in Sec. IV. Technical details of the method of solution of the Lippmann-Schwinger equation that yields our calculated scattering amplitudes that enter the Büttiker equations that yield our calculated nonlocal resistances, and also the wave functions of our transport states, are summarized in

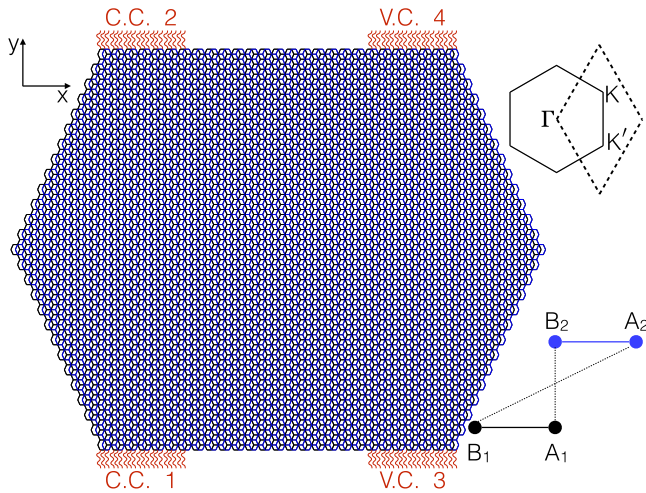


FIG. 1. Four-terminal BLG nanostructure with armchair edges. The bottom (top) layer is shown in black (blue). Each contact is composed of 40, semi-infinite 1D ideal leads (shown by red wavy lines) that are attached to both layers and connect the nanostructure to the reservoirs. The electric current flows through current contacts 1 and 2 while there is no net electric current entering or leaving the voltage contacts 3 and 4. In nonlocal resistance studies the potential difference is measured between contacts 3 and 4. Upper right inset: Two types of first Brillouin zone of bilayer graphene, hexagonal (solid) and rhombic (dotted). Lower right inset: Side view of four carbon atoms of a unit cell in bilayer graphene in AB stacking. The inversion symmetry point in the unit cell is the intersection of dotted lines.

Appendix A. The calculation of the valley-projected electronic states is described in Appendix B.

II. MODEL AND FORMALISM

To describe the bilayer graphene nanostructure with AB stacking of the two honeycomb lattice layers, the nearest neighbor tight-binding Hamiltonian H_{BLG} is employed such that

$$H_{\text{BLG}} = \sum_n \epsilon_n a_n^\dagger a_n - \sum_{\langle n,m \rangle} t_{nm} (a_n^\dagger a_m + \text{H.c.}) + \sum_{\langle n_1, m_2 \rangle} t_{n_1 m_2} (a_{n_1}^\dagger a_{m_2} + \text{H.c.}), \quad (2)$$

where ϵ_n is the on-site energy, and $t_{nm} = t = 2.7$ eV is the nearest neighbor hopping amplitude between the p_z orbitals of carbon atoms belonging to the same graphene monolayer. $t_{n_1 m_2} = 0$. It is the hopping amplitude between the p_z orbitals of nearest neighbor carbon atoms belonging to different graphene monolayers, such as carbon atoms A_1 and B_2 in the lower right inset of Fig. 1. It should be noted that the interlayer coupling [the last term on the right-hand side of Eq. (2)] is absent in the tight-binding Hamiltonian of monolayer graphene and is responsible for the difference between the electronic band structures of monolayer and bilayer graphene. To break the inversion symmetry of the structure, we have chosen $\epsilon = +V_g/2$ on the atoms of the top graphene layer and $\epsilon = -V_g/2$ on the atoms of the bottom layer to model the ef-

fects of the perpendicular electric field in the Sui *et al.* [12] and Shimazaki *et al.* [11] experiments. In contrast to monolayer graphene samples that require a hBN substrate to break the inversion symmetry and introduce a band gap around the Dirac point [10], the application of a perpendicular electric field in bilayer graphene nanostructures enables the investigation of gate tunability of nonlocal topological transport. Since precise alignment of the crystal axes of the monolayer graphene sample and hBN substrate is required during the fabrication of monolayer graphene valleytronic devices, bilayer graphene nanostructures (that do not require this alignment) may be more attractive as candidates for applications in the future technology.

A variety of different methods for calculating quantum transport coefficients within tight-binding formalisms have been developed and applied in the literature. They include Landauer mode counting applied to calculated quasi-one-dimensional band structures [24,25], recursive Green's function techniques [26–29], nonequilibrium Green's function methods [30,31], stabilized transfer matrix methods [32–34], and solution of the Lippmann-Schwinger equation [35–37], among others. In the present work we chose the Lippmann-Schwinger approach for the following reasons: It is very flexible, lending itself well to calculations of transport in the linear response regime for tight-binding models of nanostructures of many different materials, with arbitrary geometries. This versatility has made possible its application to theoretical studies of electron transport in two-dimensional (2D) semiconductor nanostructures [35], in disordered metal nanostructures [36], in ferromagnetic atomic contacts [37], in monolayer graphene nanostructures [13], in molecules bridging transition metal electrodes [38] and gold electrodes [39], in molecular spin current rectifiers [40], in arrays of molecules on silicon [41], in electrochemically gated protein nanowires [42], in single molecule nanomagnets bridging metal electrodes [43], in Fe/GaAs spin valves [44], in scanning tunneling microscopy of molecules [45], in molecular electroluminescence [46], in ballistic electron spectroscopy of buried molecules [47], in vibrational spectroscopy of molecular junctions [48], and others. The Lippmann-Schwinger equation is readily applicable to calculations of transport in nanostructures with arbitrary numbers of electrical contacts [13] when combined with the Büttiker-Landauer formalism [14]. It yields exact numerical solutions of the transport coefficients for the tight-binding model described by Eq. (2) in the linear response regime. Thus it is well suited to the present study of nonlocal resistances and valley currents in four-terminal bilayer graphene nanostructures.

According to Büttiker-Landauer theory [14] at zero temperature in the linear response regime, the current I_i in each contact i in a multiterminal nanostructure is related to the electrochemical potential of that contact μ_i and other contacts μ_j by

$$I_i = \frac{qe}{h} \left(N_i \mu_i - R_{ii} \mu_i - \sum_{j \neq i} T_{ij} \mu_j \right), \quad (3)$$

where N_i is the total number of modes supported by contact i , T_{ij} is the electron transmission probability from contact j

to contact i , and R_{ii} is the electron reflection probability from the nanostructure for contact i . In this study, each contact is represented by a group of semi-infinite one-dimensional (1D) tight-binding leads with one orbital per site, as in many previous theoretical studies of quantum transport [37–48]. These ideal leads (represented by wavy lines in Fig. 1) are attached to edge sites of both graphene layers.

In order to calculate the T_{ij} coefficients of Büttiker-Landauer theory, we have solved the Lippmann-Schwinger equation

$$|\psi^l\rangle = |\phi_o^l\rangle + G_o(E)W|\psi^l\rangle, \quad (4)$$

as is described in Appendix A. Here $|\phi_o^l\rangle$ is an eigenstate of the l th lead that is decoupled from the BLG nanostructure, $G_o(E)$ is the sum of the Green's functions of the BLG nanostructure and leads when they are decoupled, and $|\psi^l\rangle$ is the scattering eigenstate of the coupled system. W is the coupling between the BLG nanostructure and the ideal leads, i.e.,

$$W = -\sum_n t(b_n^\dagger a_n + \text{H.c.}), \quad (5)$$

where b_n^\dagger is the electron creation operator at a lead site attached to the nanostructure, a_n is the electron annihilation operator at the BLG site attached to the corresponding lead, and the hopping amplitude t is assumed to be the same as the hopping between the p_z orbitals of in-plane nearest-neighbor atoms of the BLG nanostructure. Having evaluated scattering states $|\psi^l\rangle$, the coefficients T_{ij} that enter Büttiker-Landauer theory [Eq. (3)] are given by

$$T_{ij}(E) = \sum_{l,p} |t_{lp}^{ij}|^2 \frac{v_l^i}{v_p^j}, \quad (6)$$

where t_{lk}^{ij} is the quantum transmission amplitude of an electron transmitted from the k th lead of contact j to the l th lead of contact i at energy E obtained from the scattering states $|\psi^l\rangle$. $v_{l(p)}^i = \frac{1}{\hbar} \frac{\partial \epsilon}{\partial k}$ is the electron velocity in the 1D semi-infinite lead $l(p)$ of contact $i(j)$ at energy E , and ϵ are the energy eigenvalues of the tight-binding Hamiltonian of the semi-infinite ideal lead. To calculate the four-terminal nonlocal resistance R_{NL} of a BLG nanostructure, following the calculation of electron transmission probabilities T_{ij} at the Fermi energy E_F , the Büttiker equations [Eq. (3)] are solved. Then

$$R_{\text{NL}} = \frac{\Delta V_{3,4}}{I_{1,2}}, \quad (7)$$

where $I_{1,2}$ is the electric current flowing between the current contacts 1 and 2 and $\Delta V_{3,4}$ is the potential difference between the voltage contacts 3 and 4. Here the potential difference ΔV and electrochemical potentials μ appearing in the Büttiker equations [Eq. (3)] are related by $\Delta V = \Delta\mu/q_e$.

In order to estimate the valley currents induced in a BLG nanostructure in response to the electrochemical potential differences between the contacts, the scattering states $|\psi^l\rangle$ of electrons incident from each lead l at energy E are evaluated by solving the Lippmann-Schwinger equation (4). Then the electron scattering states $|\psi^l\rangle$ are projected onto the Bloch states of BLG. As in Ref. [13], the Bloch state is assumed to belong to valley K (K') if its wave vector lies within the

upper (lower) half of the rhombic Brillouin zone represented by dotted lines in the upper right inset of Fig. 1. Further details of the projection method are described in Appendix B.

The η component of the velocity operator for electrons in BLG nanostructure is

$$v_\eta = \frac{1}{i\hbar} [\eta, H_{\text{BLG}}], \quad (8)$$

where $\eta = \sum_n \eta_n a_n^\dagger a_n$ and η_n is the η coordinate of atomic site n . Then, the valley velocity is expressed in terms of the expectation values of the velocity operator Eq. (8) with respect to projected states $|\psi_K^l\rangle$ and $|\psi_{K'}^l\rangle$ of valley K and K' , respectively. For bilayer graphene nanostructures with multiple contacts i , each at its own electrochemical potential μ_i , we define the valley velocity as an average over the contributions arising from the different contacts weighted according to the electrochemical potential differences between the contacts [13]. In particular, the weighted average velocities of electrons in valley K and K' are defined by

$$v_{K(K')\eta} = \frac{\sum_{l,i} \frac{1}{N_{li}} \langle \psi_{K(K')}^{li} | v_\eta | \psi_{K(K')}^{li} \rangle \Delta\mu_i}{\sum_{l,i} \Delta\mu_i}, \quad (9)$$

where N_{li} is an appropriate wave function normalization factor and $\Delta\mu_i$ is the electrochemical potential difference between contact i and the lowest electrochemical potential of all of the contacts. Having evaluated $v_{K\eta}$ and $v_{K'\eta}$, the weighted valley velocity is defined here as

$$v_\eta^{\text{val}} = v_{K\eta} - v_{K'\eta}. \quad (10)$$

As in Ref. [13] for monolayer graphene, the valley velocity field for the BLG nanostructure is defined by expressing the expectation value of the valley velocity given by Eqs. (9) and (10) as a sum of contributions of nearest neighbor pairs of C atoms in each layer and assigning each such contribution to the midpoint of the respective atomic pair.

From the perspective of potential valleytronic applications it is also important to know the valley accumulation and its spatial distribution in the device. For an electron in an appropriately normalized state $|\psi^l\rangle$, the valley accumulation in that state at atomic site n with carbon atom p_z orbital $|n\rangle$ is defined by $a_n^l = |\langle n | \psi_K^l \rangle|^2 - |\langle n | \psi_{K'}^l \rangle|^2$. For a nanostructure with multiple contacts in the linear response regime, the total valley accumulation A_n induced at atomic site n by changes $\Delta\mu_i$ in the electrochemical potentials μ_i of contacts i is then given by

$$A_n = \frac{1}{2\pi} \sum_{l,i} (|\langle n | \psi_K^l \rangle|^2 - |\langle n | \psi_{K'}^l \rangle|^2) \frac{\partial \zeta^l}{\partial E} \Delta\mu_i, \quad (11)$$

where it is assumed that the scattering state ψ^l originates in a semi-infinite 1D ideal tight-binding chain where it is normalized so that on site m of the chain $\langle m | \psi^l \rangle = e^{i\zeta^l m} + r^l e^{-i\zeta^l m}$ where r^l is the reflection amplitude of the incoming state $|\psi^l\rangle$ from the nanostructure back into ideal lead l , and E is the energy eigenvalue corresponding to state ψ^l .

It is then natural to define valley accumulation susceptibilities per carbon atom as

$$C_{ni} = e^2 \frac{\partial A_n}{\partial \Delta\mu_i}, \quad (12)$$

where the factor e^2 is introduced so that C_{ni} has the units of capacitance. Henceforth we shall refer to the C_{ni} as ‘‘partial valley capacitances.’’ For a multiterminal device in the linear response regime we characterize the total valley accumulation due to the contributions of all of the contacts by a total valley capacitance defined by

$$C_n = e^2 \frac{A_n}{\Delta\mu_{\max}}, \quad (13)$$

where $\Delta\mu_{\max}$ is the largest of the $\Delta\mu_i$ over all of the contacts i .

We find the valley capacitances to often have differing signs at the different atoms in the unit cell, and therefore to better characterize the overall magnitude of the valley accumulation we define an averaged valley capacitance by

$$C_{\text{av}}(x,y) = \frac{C_l + C_k}{2}, \quad (14)$$

where $(x,y) = [(x_l + x_k)/2, (y_l + y_k)/2]$, and C_l and C_k are the total valley capacitances calculated for two carbon atoms belonging to the same graphene layer and in the same unit cell. Inspection of spatial maps of these cell-averaged capacitances facilitates developing an understanding of the relationship between valley currents and valley accumulation, as will be seen below.

III. RESULTS

The results of our calculation of the four-terminal nonlocal resistance obtained by the application of Büttiker-Landauer theory [Eq. (3)] at zero temperature in the linear response regime are shown in Fig. 2(a) as a function of the Fermi energy for different values of the gate voltage. As is seen in Fig. 2(a), enhancement of the nonlocal resistance R_{NL} occurs near the energy of Dirac point $E_F = 0$. The breaking of inversion symmetry of the BLG nanostructure by application of a potential $+V_g/2$ to the top layer and $-V_g/2$ to the bottom layer leads to the striking enhancement of the nonlocal resistance. As the gate voltage increases the maximum value of R_{NL} which occurs at $E_F = 0$ also increases implying that nonlocal electron transport in the BLG nanostructure is gate tunable. Furthermore, as can be seen in Fig. 2(a), when the Fermi energy is well away from the energy of Dirac point, the symmetry breaking does not result in large nonlocal resistances R_{NL} .

The results for the normalized valley velocity v_x^{val}/v_y as a function of the Fermi energy for different values of gate voltage V_g are presented in Figs. 2(b)–2(d). The computed weighted valley velocities in the x and y directions are normalized by the weighted electron velocity in the y direction v_y . [Since the net electric current flows between the current contacts 1 and 2 (shown in Fig. 1) the weighted average velocity of electrons in the x direction v_x is near zero within numerical error, as expected since the net electric current points in the y direction.] In Fig. 2(b) the computed normalized x component of valley velocity or valley current ($v_x^{\text{val}}/v_y = I_x^{\text{val}}/I$) is shown for different values of the gate voltage where I is the total electric current flowing through the nanostructure. It is seen that the x component of valley current I_x^{val} peaks when the Fermi energy passes the energy of Dirac point. It should be

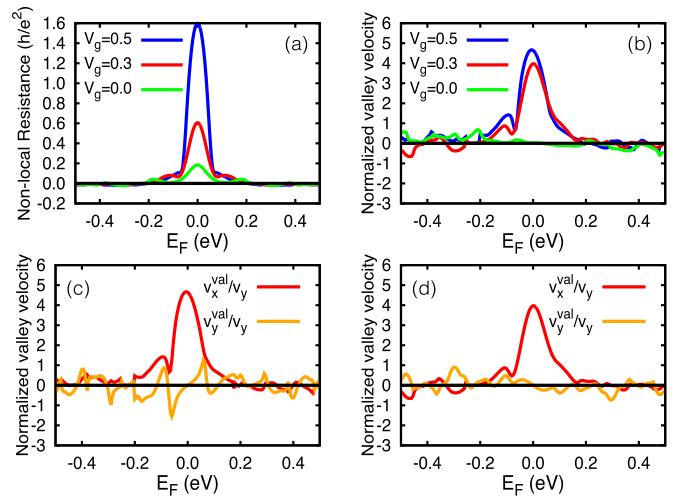


FIG. 2. (a) Calculated nonlocal resistance R_{NL} [Eq. (7)] of the nanostructure of Fig. 1 in the linear response regime at zero temperature for different values of the gate voltage $V_g = 0$ eV (green), $V_g = 0.3$ eV (red), and $V_g = 0.5$ eV (blue) as a function of Fermi energy E_F . (b) Normalized valley velocity v_x^{val}/v_y of the BLG nanostructure for different values of the gate voltage as a function of Fermi energy when the net current flows between current contacts 1 and 2. (c) Comparison of the x and y components of the normalized valley velocity as a function of Fermi energy at $V_g = 0.5$ eV. (d) Comparison of the x and y components of normalized valley velocity as a function of Fermi energy at $V_g = 0.3$ eV.

pointed out that when the inversion symmetry breaking is absent ($V_g = 0$) the evaluated valley current in the x direction is zero at $E_F = 0$, while its value exceeds the value of electric current flowing through the nanostructure in the presence of inversion symmetry breaking for all of the values of $V_g \neq 0$ that are shown. A comparison of the x and y components of normalized valley velocities is presented in Figs. 2(c) and 2(d). Based on these results the y component of valley current approaches zero as the Fermi energy passes the energy of Dirac point. To summarize, the valley currents flow through the BLG nanostructure mainly in the x direction. Also, the x and y components of valley current are relatively small in the presence or absence of inversion symmetry breaking if the Fermi energy is well away from the Dirac point.

For comparison, we have also calculated the nonlocal resistance and valley current in the linear response regime for a model nanostructure whose dimensions (including the widths of the contacts) are one half of those of the nanostructure considered in Figs. 1 and 2. The simulation results, show that when the gate voltage $V_g = 0.3$ eV, the nonlocal resistance of the smaller nanostructure is smaller by a factor of ~ 16 at $E_F = 0$. However, the calculated normalized valley current in the x direction is smaller by a factor of ~ 2.5 for the smaller sample. The valley current in the y direction is still equal to zero when the Fermi level passes the energy of the Dirac point.

Returning to the bilayer graphene nanostructure in Fig. 1, in Fig. 3(a) we show the gate tunability of the valley velocity in the x direction (v_x^{val}/v_y) and of the nonlocal resistance at zero Fermi energy (the energy at which the maximum values of the valley current and nonlocal resistance occur)

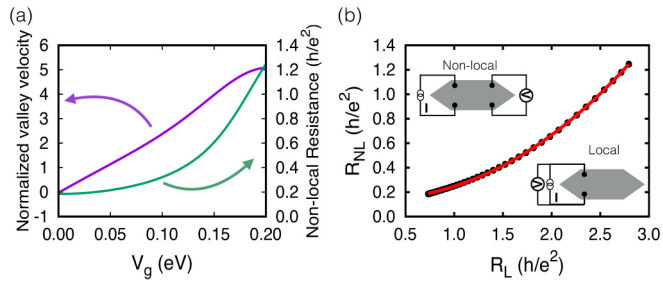


FIG. 3. (a) The normalized valley velocity (v_x^{val}/v_y) (purple line) and nonlocal resistance R_{NL} (green line) of the bilayer graphene nanostructure as a function of gate voltage at zero Fermi energy $E_F = 0$. (b) The scaling relation between the local and nonlocal resistance as the gate voltage varies from 0 to 0.2 eV. Red line is the power law $R_{NL} \sim R_L^\alpha$ fitted to the simulation data. Upper left inset: The configuration of nonlocal resistance measurements. Lower right inset: The configuration of local resistance measurements.

as the gate voltage V_g varies. As can be seen, the valley current (purple line) increases from zero (when the inversion symmetry is absent, i.e., $V_g = 0$) to a value of five times larger than the electric current. The normalized valley current increases linearly as the gate voltage increases for low values of the gate voltage (i.e., $0 < V_g < 0.1$ eV). By contrast, the computed nonlocal resistance R_{NL} (green line) of the

BLG nanostructure increases quadratically (from a nonzero value at $V_g = 0$) as a function of gate voltage. Deviations from these scaling relations of valley current and nonlocal resistance occur for higher values of the gate voltage (i.e., $V_g > 0.1$ eV). The relationship between the local and nonlocal resistances is investigated in Fig. 3(b) as the gate voltage varies from 0 to 0.2 eV at zero Fermi energy. The local resistance R_L is computed when the electric current flows through the nanostructure between current contacts 1 and 2 and the potential difference is measured between the same contacts ($R_L = \Delta V_{1,2}/I_{1,2}$). According to Fig. 3(b), the power-law relation $R_{NL} \sim R_L^\alpha$ is satisfied with $\alpha = 2.19$. Deviation of α from the experimental results $\alpha = 3$ [11] and $\alpha = 2.77$ [12] may result from the difference between ballistic transport system investigated in this paper and diffusive transport in the experiments. As reported [12], the power α differs in different samples as a consequence of disorder in the samples.

The total valley capacitance [Eq. (13)] map of the bottom layer of the BLG nanostructure is presented in Fig. 4(a) for the net current flowing between current contacts 1 and 2. The blue disks indicate a positive total valley capacitance C_n and red disks represent negative C_n . As can be seen in Fig. 4(a), the valley capacitance is stronger on sites close to the contacts from which electrons enter the nanostructure even if no net current flows through that contact. It should also be noted that the total valley capacitance in the top layer (not shown) exhibits

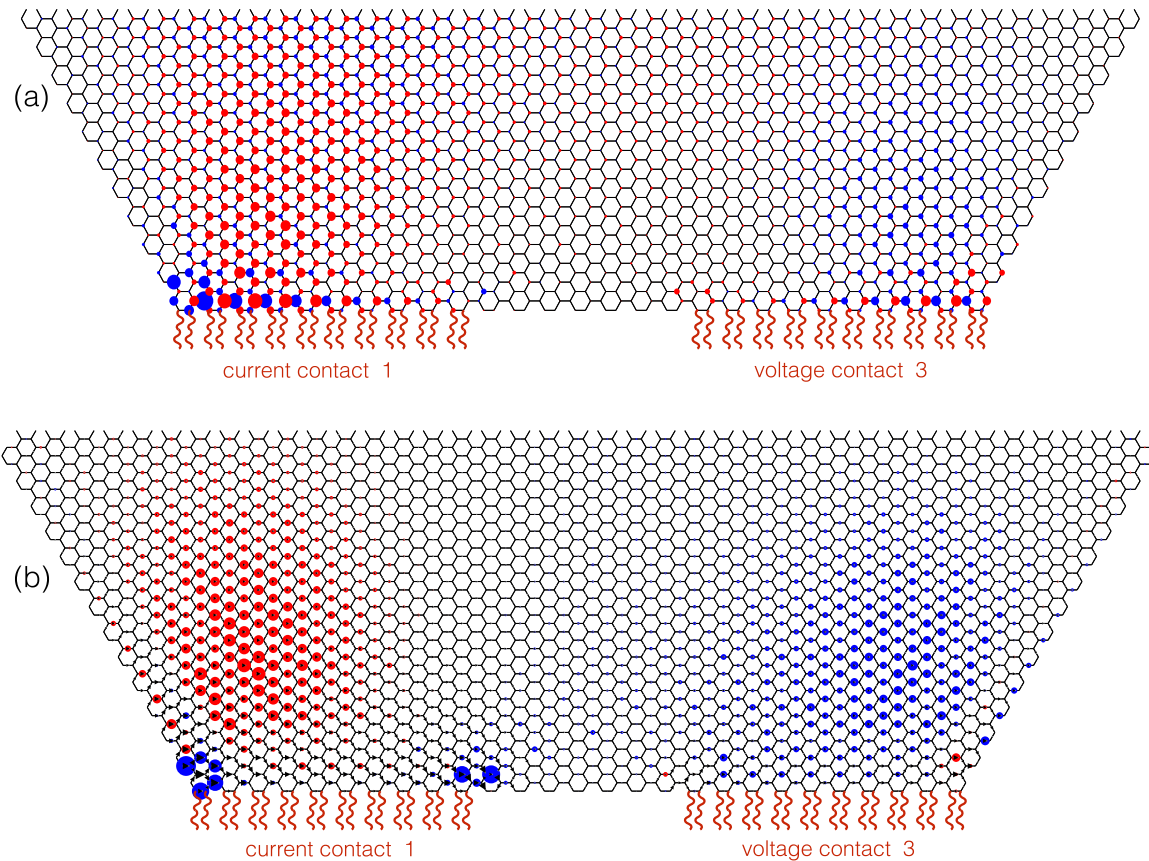


FIG. 4. The calculated total valley capacitance, valley velocity field, and unit cell-averaged valley capacitance of the bottom layer of a bilayer graphene nanostructure when the net electric current flows between current contact 1 and 2 at $V_g = 0.15$ eV and $E_F = 0$. (a) The total valley capacitance [Eq. (13)] is represented by blue (red) disks when the on-site valley accumulation is positive (negative). (b) The valley velocity field (black arrows) and average valley capacitance (red and blue disks), Eq. (14).

similar behavior to that for the bottom layer of the BLG nanostructure.

In Fig. 4(b) the spatial distribution of the valley velocity and average valley capacitance [Eq. (14)] in each unit cell of the bottom layer for broken inversion symmetry ($V_g = 0.3$ eV) is represented by arrows (black) and disks (red and blue), respectively. As can be seen the valley current is chiral and directed from left to right along the lower boundary of the nanostructure, while along the opposite boundary (not shown) the valley current is also chiral but weaker and travels in opposite direction, from right to left. The overall directions of the valley velocities along the lower and upper boundaries of the BLG nanostructure reverse if the sign of V_g is changed. Apart from at a few exceptional sites near the ends of contacts 1 and 3, the cell-averaged valley capacitance in Fig. 4(b) exhibits a dipolar distribution, being negative (red) on the left and positive (blue) on the right. The maximum absolute value of the cell-averaged valley capacitance $|C_{av}(x, y)|$ is $\sim 0.12 \times 10^{-22}$ F/atom. For comparison, a classical parallel plate capacitor with a 3.1 Å plate spacing would have a conventional capacitance of $\sim 7 \times 10^{-22}$ F per atomic area of graphene.

The dipolar character of the average valley capacitance in Fig. 4(b) [the negative (red) region on the left and positive (blue) region on the right] has physical (and potentially practical) significance. It indicates that the valley current that flows from left to right in fact transports the valley degree of freedom across the nanostructure and results in a significant valley imbalance between these two regions of the nanostructure, despite the fact that the electron crystal momentum is not conserved when an electron scatters from a boundary of the nanostructure.

The computed average valley capacitance is negligible in the absence of inversion symmetry breaking and grows as the applied gate voltage increases. It should be noted that the average valley capacitance in the unit cell and valley velocity field in the top layer are similar to those in the bottom layer that are shown in Fig. 4(b).

IV. CONCLUSIONS

The present study has investigated the nonlocal resistance, valley currents, and average valley capacitance of four-terminal bilayer graphene nanostructures from the perspective of scattering theory in the insulating regime. The calculations have been carried out in the limit where the effect of the electric field that drives electrons has been sent to zero. As a consequence, in the linear response regime, the interpretation of the valley currents by application of the anomalous velocity term is not appropriate. The valley currents calculated here within the formalism of scattering theory are not due to the acceleration of electrons in an electric field when the inversion symmetry is broken (nonzero Berry curvature), but result from nonadiabatic injection of electrons into the BLG nanostructure through the contacts. The valley currents are maximal in the insulating regime where the Fermi energy is in a spectral gap close to the energy of Dirac point, so that electron transport is only possible by quantum tunneling. Consequently, the calculated valley currents are strongest in the BLG nanostructure with broken inversion symmetry close to the contacts from which electrons enter the nanostructure even if

there is no net electric current passing through those contacts (the case of voltage contacts of the BLG nanostructure). For the Fermi energies near the energy of the Dirac point, the valley currents are several times larger than the electric current passing through the current contacts when the inversion symmetry is broken. On the other hand, if the Fermi energy is well away from the Dirac point, the impact of inversion symmetry breaking on the overall magnitude of the valley currents is not significant. Furthermore, mapping the average valley capacitance calculated in the BLG nanostructure with broken inversion symmetry reveals a dipolar distribution that results from the presence valley currents so that the average valley capacitance increases in the direction of valley currents. The evaluated scaling relation between local and nonlocal resistances as the gate voltage varies, shows that the diffusive power law is satisfied in the ballistic linear response regime although with a modified exponent. The valley currents and average valley accumulation in bilayer graphene are electrically controllable by means of a perpendicular electric field which is an advantage for the application of bilayer graphene over monolayer graphene nanostructures. It should be noted that the valley currents and average valley capacitances in both layers of the bilayer graphene have similar characteristics.

ACKNOWLEDGMENTS

This research was supported by NSERC, Westgrid, CIFAR, and Compute Canada.

APPENDIX A: SOLUTION OF THE LIPPMANN-SCHWINGER EQUATION

In this Appendix we discuss the evaluation of the decoupled Green's function $G_c(E)$ that enters the Lippmann-Schwinger equation (4), the method of solution of the Lippmann-Schwinger equation in the tight-binding formalism, and how this solution relates to the Büttiker equations and the electronic transport states.

The Green's function of each decoupled contact represented by a group of semi-infinite one-dimensional leads depicted in Fig. 1 is the sum of the Green's functions of the individual decoupled leads associated with that contact. The energy of an electron in a one-dimensional lead with one atomic orbital per site in the tight-binding model is $E_k = \epsilon + 2\tau \cos(ka)$, where ϵ is the on-site energy (equal to the on-site energy of the carbon atom attached to that lead), τ is the hopping amplitude between the nearest neighbors [$|\tau| = t$ in the bilayer graphene tight-binding Hamiltonian Eq. (2)], and a is the nearest neighbor spacing between the atomic sites in one-dimensional lead. Therefore, the electron wave function in the l th lead when it is decoupled from the graphene nanostructure has the form

$$|\phi_c\rangle = \frac{1}{\sqrt{2N}} \sum_{n_l=1}^N (e^{ikn_l a} - e^{-ikn_l a}) |n_l\rangle, \quad (\text{A1})$$

where N is the total number of atoms (assumed to be very large) in the one-dimensional lead, and $|n_l\rangle$ is the n th atomic orbital state in that lead. Then the decoupled Green's function

of the l th lead is

$$\begin{aligned} G_{\circ}^l(E) &= \frac{1}{E - H_{\circ}^l + i\delta} \\ &= \sum_{n_l n_l'} (G_{\circ})_{n_l n_l'}^l |n_l\rangle \langle n_l'|, \end{aligned} \quad (\text{A2})$$

where H_{\circ}^l is the Hamiltonian of the l th decoupled 1D lead and $(G_{\circ})_{n_l n_l'}^l = \langle n_l | G_{\circ}^l(E) | n_l' \rangle$. For our purposes this decoupled Green's function needs to be evaluated only at an end site ($n_l = \pm 1$) where the l th lead will ultimately be attached to the BLG nanostructure. Its corresponding matrix element can be written as

$$(G_{\circ})_{\pm 1, \pm 1}^l = \frac{1}{2\pi} \int_0^{2\pi} dk \frac{1 - e^{2ik}}{\{E - [\epsilon + 2\tau \cos(k)] + i\delta\}}. \quad (\text{A3})$$

By application of residue theorem, the Green's function of the decoupled semi-infinite one-dimensional l th lead is

$$(G_{\circ})_{\pm 1, \pm 1}^l = \frac{i}{2\tau} \frac{(1 - e^{2ika})}{\sin(ka)}. \quad (\text{A4})$$

It should be noted that in derivation of Eq. (A3) we have used the conversion of summation to the integral as $\sum_k \rightarrow \frac{L}{2\pi} \int_{-\frac{\pi}{a}}^{\frac{\pi}{a}} dk$. Then the Green's function of decoupled bilayer graphene nanostructure can be written as

$$G_{\circ}^{\text{BLG}}(E) = \sum_{\alpha} \frac{|\alpha\rangle \langle \alpha|}{E - \epsilon_{\alpha} + i\delta}, \quad (\text{A5})$$

where ϵ_{α} are the energy eigenvalues and $|\alpha\rangle$ are the corresponding eigenstates of the BLG Hamiltonian (2) decoupled from the leads. ϵ_{α} and $|\alpha\rangle$ are calculated numerically by diagonalizing the BLG Hamiltonian.

To evaluate the quantum transmission amplitude of an electron t_{lk}^{ij} , transmitted from the k th lead of contact j to the l th lead of contact i at energy E , we expand the scattering state $|\psi^l\rangle$ of electrons that enters Eq. (4) in terms of atomic orbitals

$$\begin{aligned} |\psi^l\rangle &= \sum_{n_l = -\infty}^{-1} (e^{ik^l n_l a} + r_l e^{-ik^l n_l a}) |n_l\rangle \\ &+ \sum_i C_i |c_i\rangle + \sum_{\beta} \sum_{n_{\beta}=1}^{\infty} t_{\beta,l} e^{ik^{\beta} n_{\beta} a} |n_{\beta}\rangle, \end{aligned} \quad (\text{A6})$$

where l specifies the 1D lead from which the electron is injected into the BLG nanostructure (belongs to one of the contacts in Fig. 1), r_l is the amplitude for reflection of the electron back into the same 1D lead l , i specifies the sites of the carbon atoms in the nanostructure, and β specifies the 1D leads into which the electron is transmitted with amplitude $t_{\beta,l}$. By inserting Eqs. (A3), (A5), and (A6) into Eq. (4), and applying $\langle c_i |$, $\langle -1_l |$ and $\langle +1_{\beta} |$ to the result, the Lippmann-Schwinger equation becomes a system of linear equations. This is solved numerically to find the quantum transmission amplitudes $t_{\beta,l}$ and reflection amplitudes r_l that are required to obtain the

transmission and reflection coefficients T_{ji} and R_{ii} that enter the Büttiker Eq. (3) that is used to calculate the nonlocal resistance R_{NL} . The solution of the above system of linear equations also yields the coefficients C_i in Eq. (A6) that define the electronic transport states $|\psi^l\rangle$ within the BLG nanostructure.

APPENDIX B: VALLEY-PROJECTED STATES

In order to evaluate the valley currents in the bilayer graphene nanostructure, the scattering states of electrons $|\psi^l\rangle$ are projected onto crystal Bloch states, which can be written as

$$\begin{aligned} |\psi_{\mathbf{k}}^{\alpha}\rangle &= \frac{1}{\sqrt{N}} \sum_{i=1}^N e^{i\mathbf{k}\cdot\mathbf{R}_i} [c_{A_1}^{\alpha}(\mathbf{k}) |p_{z,i}^{A_1}\rangle + c_{B_1}^{\alpha}(\mathbf{k}) |p_{z,i}^{B_1}\rangle \\ &+ c_{A_2}^{\alpha}(\mathbf{k}) |p_{z,i}^{A_2}\rangle + c_{B_2}^{\alpha}(\mathbf{k}) |p_{z,i}^{B_2}\rangle], \end{aligned} \quad (\text{B1})$$

where $\alpha = 1, \dots, 4$ denotes the different Bloch states having wave vector \mathbf{k} , N is the total number of unit cells in the BLG nanostructure, \mathbf{R}_i are the Bravais lattice vectors of bilayer graphene, and $|p_{z,i}^{A_1}\rangle, |p_{z,i}^{A_2}\rangle, |p_{z,i}^{B_1}\rangle, |p_{z,i}^{B_2}\rangle$ are the carbon atomic orbitals in the i th unit cell. Then the rhombic Brillouin zone of bilayer graphene represented in Fig. 1 is divided into two parts and the Bloch state is assumed to belong to the valley K (K') if its wave vector lies within the upper (lower) half of the rhombic Brillouin zone. Hence, the projected states are calculated as

$$\begin{aligned} |\psi_K^l\rangle &= A \sum_{\alpha, \mathbf{k} \in K} |\psi_{\mathbf{k}}^{\alpha}\rangle \langle \psi_{\mathbf{k}}^{\alpha} | \psi^l \rangle, \\ |\psi_{K'}^l\rangle &= A \sum_{\alpha, \mathbf{k} \in K'} |\psi_{\mathbf{k}}^{\alpha}\rangle \langle \psi_{\mathbf{k}}^{\alpha} | \psi^l \rangle. \end{aligned} \quad (\text{B2})$$

The Bloch states $|\psi_{\mathbf{k}}^{\alpha}\rangle$ are defined on a continuum in \mathbf{k} space. However, in practice the sums in Eq. (B2) are evaluated on a mesh of \mathbf{k} points, the number of \mathbf{k} points in the mesh being chosen large enough for convergence of the valley currents being calculated with the help of the valley-projected states. Thus appropriate normalization of the projected states is necessary. In Eq. (B2) $A = \frac{\text{number of unit cells}}{\text{number of mesh points}}$ is the required normalization factor, and the sums run over the mesh points belonging to the corresponding valley K or K' . Note that the Bloch states of a bilayer graphene crystal with wave vector \mathbf{k} can be written as linear combinations of Bloch states (with the same wave vector \mathbf{k}) of the two monolayer graphene crystals that comprise the bilayer. Therefore, for the purpose of projecting the scattering states of electrons $|\psi^l\rangle$ onto the subspace of crystal Bloch states with wave vector \mathbf{k} , Bloch states of a pair of decoupled graphene monolayer crystals can be used instead of Bloch states of the bilayer in Eqs. (B1) and (B2), with equivalent results.

This projection method was used in the present work.

[1] K. S. Novoselov, A. K. Geim, S. V. Morozov, D. Jiang, Y. Zhang, S. V. Dubonos, I. V. Grigorieva, and A. A. Firsov, Electric

field effect in atomically thin carbon films, *Science* **306**, 666 (2004).

- [2] K. S. Novoselov, E. McCann, S. V. Morozov, V. I. Fal'ko, M. I. Katsnelson, U. Zeitler, D. Jiang, F. Schedin, and A. K. Geim, Unconventional quantum Hall effect and Berry's phase of 2π in bilayer graphene, *Nat. Phys.* **2**, 177 (2006).
- [3] T. Ohta, A. Bostwick, T. Seyller, K. Horn, and E. Rotenberg, Controlling the electronic structure of bilayer graphene, *Science* **313**, 951 (2006).
- [4] S. Ghosh, W. Bao, D. L. Nika, S. Subrina, P. E. Pokatilov, C. N. Lau, and A. A. Balandin, Dimensional crossover of thermal transport in few-layer graphene, *Nat. Mater.* **9**, 555 (2010).
- [5] A. A. Balandin and A. Alexander, Thermal properties of graphene and nanostructured carbon materials, *Nat. Mater.* **10**, 569 (2011).
- [6] R. R. Nair, P. Blake, A. N. Grigorenko, K. S. Novoselov, T. J. Booth, T. Stauber, N. M. R. Peres, and A. K. Geim, Fine structure constant defines visual transparency of graphene, *Science* **320**, 1308 (2008).
- [7] D. Xiao, M.-C. Meng, and Q. Niu, Berry phase effects on electronic properties, *Rev. Mod. Phys.* **82**, 1959 (2010).
- [8] R. Karplus and J. M. Luttinger, Hall effect in ferromagnetics, *Phys. Rev.* **95**, 1154 (1954).
- [9] Y. D. Chong, Berry's phase and the anomalous velocity of Bloch wavepackets, *Phys. Rev. B* **81**, 052303 (2010).
- [10] R. V. Gorbachev, J. C. W. Song, G. L. Yu, A. V. Kretinin, F. Withers, Y. Cao, A. Mishchenko, I. V. Grigorieva, K. S. Novoselov, L. S. Levitov, and A. K. Geim, Detecting topological currents in graphene superlattices, *Science* **346**, 448 (2014).
- [11] Y. Shimazaki, M. Yamamoto, I. V. Borzenets, K. Watanabe, T. Taniguchi, and S. Tarucha, Generation and detection of pure valley current by electrically induced Berry curvature in bilayer graphene, *Nat. Phys.* **11**, 1032 (2015).
- [12] M. Q. Sui, G. R. Chen, L. G. Ma, W. Y. Shan, D. Tian, K. Watanabe, T. Taniguchi, X. F. Jin, W. Yao, D. Xiao, and Y. B. Zhang, Gate-tunable topological valley transport in bilayer graphene, *Nat. Phys.* **11**, 1027 (2015).
- [13] G. Kirczenow, Valley currents and nonlocal resistances of graphene nanostructures with broken inversion symmetry from the perspective of scattering theory, *Phys. Rev. B* **92**, 125425 (2015).
- [14] M. Büttiker, Four-Terminal Phase-Coherent Conductance, *Phys. Rev. Lett.* **57**, 1761 (1986).
- [15] D. A. Abanin, A. V. Shytov, L. S. Levitov, and B. I. Halperin, Nonlocal charge transport mediated by spin diffusion in the spin Hall effect regime, *Phys. Rev. B* **79**, 035304 (2009).
- [16] D. Xiao, W. Yao, and Q. Niu, Valley-Contrasting Physics in Graphene: Magnetic Moment and Topological Transport, *Phys. Rev. Lett.* **99**, 236809 (2007).
- [17] A. Rycerz, J. Tworzydło, and C. W. J. Beenakker, Valley filter and valley valve in graphene, *Nat. Phys.* **3**, 172 (2007).
- [18] T. Nakanishi, M. Koshino, and T. Ando, Transmission through a boundary between monolayer and bilayer graphene, *Phys. Rev. B* **82**, 125428 (2010).
- [19] D. Gunlycke and C. T. White, Graphene Valley Filter Using a Line Defect, *Phys. Rev. Lett.* **106**, 136806 (2011).
- [20] T. Oka and H. Aoki, Photovoltaic Hall effect in graphene, *Phys. Rev. B* **79**, 081406(R) (2009).
- [21] D. S. L. Abergel and T. Chakraborty, Generation of valley polarized current in bilayer graphene, *Appl. Phys. Lett.* **95**, 062107 (2009).
- [22] L. E. Golub, S. A. Tarasenko, M. V. Entin, and L. I. Magarill, Valley separation in graphene by polarized light, *Phys. Rev. B* **84**, 195408 (2011).
- [23] D. R. da Costa, A. Chaves, S. H. R. Sena, G. A. Farias, and F. M. Peeters, Valley filtering using electrostatic potentials in bilayer graphene, *Phys. Rev. B* **92**, 045417 (2015).
- [24] G. Kirczenow, in *The Oxford Handbook of Nanoscience and Technology, Volume I: Basic Aspects*, edited by A. V. Narlikar and Y. Y. Fu (Oxford University Press, Oxford, 2010), Chap. 4.
- [25] N. M. R. Peres, A. H. C. Neto, and F. Guinea, Conductance quantization in mesoscopic graphene, *Phys. Rev. B* **73**, 195411 (2006).
- [26] P. A. Lee and D. S. Fisher, Anderson Localization in Two Dimensions, *Phys. Rev. Lett.* **47**, 882 (1981).
- [27] A. MacKinnon, The calculation of transport properties and density of states of disordered solids, *Z. Phys. B* **59**, 385 (1985).
- [28] T. Ando, Quantum point contacts in magnetic fields, *Phys. Rev. B* **44**, 8017 (1991).
- [29] H. Xu, T. Heinzel, M. Evaldsson, and I. V. Zozoulenko, Magnetic barriers in graphene nanoribbons: Theoretical study of transport properties, *Phys. Rev. B* **77**, 245401 (2008).
- [30] S. Datta, *Electronic Transport in Mesoscopic Systems* (Cambridge University Press, Cambridge, UK, 1997).
- [31] R. Lake, G. Klimeck, R. C. Bowen, and D. Jovanovic, Single and multiband modeling of quantum electron transport through layered semiconductor devices, *J. Appl. Phys.* **81**, 7845 (1997).
- [32] T. Usuki, M. Saito, M. Takatsu, R. A. Kiehl, and N. Yokoyama, Numerical analysis of ballistic-electron transport in magnetic fields by using a quantum point contact and a quantum wire, *Phys. Rev. B* **52**, 8244 (1995).
- [33] R. A. Akis, D. K. Ferry, and J. P. Bird, Magnetotransport fluctuations in regular semiconductor ballistic quantum dots, *Phys. Rev. B* **54**, 17705 (1996).
- [34] G. Kirczenow, B. L. Johnson, P. J. Kelly, C. Gould, A. S. Sachrajda, Y. Feng, and A. Delage, Resonance patterns of an antidot cluster: From classical to quantum ballistics, *Phys. Rev. B* **56**, 7503 (1997).
- [35] S. Nonoyama, A. Nakamura, Y. Aoyagi, T. Sugano, and A. Okiji, Numerical study of the interference effects of electron waves scattered by impurities or slits in a quasi-one-dimensional system, *Phys. Rev. B* **47**, 2423 (1993).
- [36] G. Kirczenow, Why are large persistent currents observed in small gold rings?, *J. Phys.: Condens. Matter* **7**, 2021 (1995).
- [37] H. Dalglish and G. Kirczenow, Theoretical study of spin-dependent electron transport in atomic Fe nanocontacts, *Phys. Rev. B* **72**, 155429 (2005).
- [38] H. Dalglish and G. Kirczenow, A new approach to the realization and control of negative differential resistance in single-molecule nanoelectronic devices: Designer transition metal-thiol interface states, *Nano Lett.* **6**, 1274 (2006).
- [39] A. Saffarzadeh, F. Demir, and G. Kirczenow, Mechanism of the enhanced conductance of a molecular junction under tensile stress, *Phys. Rev. B* **89**, 045431 (2014).
- [40] H. Dalglish and G. Kirczenow, Spin-current rectification in molecular wires, *Phys. Rev. B* **73**, 235436 (2006).
- [41] G. Kirczenow, P. G. Piva, and R. A. Wolkow, Modulation of electrical conduction through individual molecules on silicon by the electrostatic fields of nearby polar molecules: Theory and experiment, *Phys. Rev. B* **80**, 035309 (2009).

- [42] D. M. Cardamone and G. Kirczenow, Electrochemically gated oligopeptide nanowires bridging gold electrodes: Novel bio-nanoelectronic switches operating in aqueous electrolytic environments, *Nano Lett.* **10**, 1158 (2010).
- [43] F. R. Renani and G. Kirczenow, Tight-binding model of Mn 12 single-molecule magnets: Electronic and magnetic structure and transport properties, *Phys. Rev. B* **85**, 245415 (2012).
- [44] S. Majumder, B. Kardasz, G. Kirczenow, A. S. Thorpe, and K. L. Kavanagh, Lateral spin injection and detection through electrodeposited Fe/GaAs contacts, *Semicond. Sci. Technol.* **28**, 035003 (2013).
- [45] J. Buker and G. Kirczenow, Two-probe theory of scanning tunneling microscopy of single molecules: Zn (II)-etioporphyrin on alumina, *Phys. Rev. B* **72**, 205338 (2005).
- [46] J. Buker and G. Kirczenow, Understanding the electroluminescence emitted by single molecules in scanning tunneling microscopy experiments, *Phys. Rev. B* **78**, 125107 (2008).
- [47] G. Kirczenow, Ballistic electron spectroscopy of individual buried molecules, *Phys. Rev. B* **75**, 045428 (2007).
- [48] F. Demir and G. Kirczenow, Communication: Identification of the molecule–metal bonding geometries of molecular nanowires, *J. Chem. Phys.* **134**, 121103 (2011).